Supporting Information

for

Explicit Spatio-Temporal Simulation of Receptor-G Protein Coupling in Rod Cell Disk Membranes

Johannes Schöneberg[1], Martin Heck[2], Klaus-Peter Hofmann[2], Frank Noé[1]

[1] Department of Mathematics, Computer Science and Bioinformatics, FU Berlin, Arnimallee 6, 14195 Berlin, Germany
[2] Institut für Medizinische Physik und Biophysik, Charité - Universitätsmedizin Berlin, Charitéplatz 1, 10117 Berlin, Germany

Table S1: Kinetic parameters of G activation

Parameter		Kinetic definition [a]	Value [b]
$\frac{V_{\max}}{R^*}$	(forward) turnover number	$\frac{k_2 k_4}{(k_2 + k_4)}$	594 ± 17 s^{-1}
K_m^G	Michaelis constant for Gt	$\frac{k_4(k_{-1} + k_2)}{k_1(k_2 + k_4)}$	2182 ± 110 μm^{-2}
K_m^{GTP}	Michaelis constant for GTP	$\frac{k_2(k_{-3} + k_4)}{k_3(k_2 + k_4)}$	231 ± 10 µM
K_d^G	dissociation constant for Gt	$\frac{k_{-1}}{k_1}$	534 ± 257 μm^{-2}
K_d^{GDP}	dissociation constant for GDP	$\frac{k_2}{k_{-2}}$	274 ± 37 µM

[a] see (1) for derivation; for assignment of the individual rate constants see Fig. 1A and Table 1.

[b] Values are taken from (2) and represent the experimentally obtained values corrected for the fraction of active receptor relative to the total amount of light-activated rhodopsin.

Table S2: Initial concentrations of the reactants in ODE-fitting

Species	Initial concentration
$[M1]_n^0$	5.7 μm^{-2}
$[R^*]_n^0$	0
$[G]_1^0$	273 μm^{-2} (a)
$[G]_2^0$	1265 μm^{-2} (a)
$[G]_3^0$	2525 μm^{-2} (a)
$[G]_4^0$	5444 μm^{-2} (a)
$[G]_5^0$	655 μm^{-2}
$[G]_6^0$	2160 μm^{-2}
$[G]_7^0$	3706 μm^{-2}
$[R^*G]_n^0$	0
$[R^*G_0]_n^0$	0
$[R^*G^*]_n^0$	0
$[G^*]_n^0$	0
$[G^*_{sol}]_n^0$	0

(a) G concentrations also used for ReaDDy

Table S3: Initial estimation of selected rate constants

Rate constant	Description	Initial estimation
k_1	Rate of R*G complex formation	$0.27\ \mu m^2 s^{-1} < k_1 < 0.36\ \mu m^2 s^{-1}$
k_{-1}	Rate of R*G complex dissociation	$145\ s^{-1} < k_{-1} < 192\ s^{-1}$
k_2	Rate of GDP release from R*G complex	$> 594\ s^{-1}$
k_{-2}	Rate of GDP uptake by R*G complex	$> 2.2\ \mu M^{-1} s^{-1}$
k_3	Rate of GTP uptake by R*G complex	$> 2.57\ \mu M^{-1} s^{-1}$
k_{-3}	Rate of GTP release from R*G* complex	$< 594\ s^{-1}$
k_4	Rate of R*G* complex dissociation	$> 594\ s^{-1}$

Table S4: Estimation of rate constants

Rate constant	Set A	Set B
k_{M2}	$35.4\ s^{-1}$	
k_{-M2}	$14.4\ s^{-1}$	
k_1	$0.36\ \mu m^2 s^{-1}$	$0.27\ \mu m^2 s^{-1}$
k_{-1}	200	140
k_2	$600\ s^{-1}$	$60000\ s^{-1}$
$k_{-2}^{GDP} = k_{-2}$ [GDP]	$2.6\ \mu M^{-1} s^{-1}$ [GDP]	$260\ \mu M^{-1} s^{-1}$ [GDP]
$k_3^{GTP} = k_3$ [GTP]	$2.6\ \mu M^{-1} s^{-1}$ [GTP]	$5.1\ \mu M^{-1} s^{-1}$ [GTP]
k_{-3}	$600\ s^{-1}$	
k_4	$60000\ s^{-1}$	$600\ s^{-1}$
k_{-4}	$0\ s^{-1}$	
k_{sol}	$10000\ s^{-1}$	
k_{-sol}	$0\ s^{-1}$	

Reaction rates derived from ODE-fitting for the reaction system given in Eqs. (1)-(3) in Fig. 1.

Estimation of the rate constants and ODE-model

Activation of Gt is accompanied *in vitro* by a complete release of the active Gtα-subunit and

a partial release of the Gtβγ-subunit from the disk membranes. Accordingly, light-induced activation of Gt can be monitored in real time by probing the resulting loss of mass of the disk vesicles as a decrease of near infrared light scattering ("dissociation signal"; (2-4)). In a previous study, kinetic parameters for the individual steps of Gt activation (Table S1) were quantified by a rate analysis of dissociation signals titrated with Gt, GTP and GDP (2). In the following, these kinetic parameters were used for a rough initial estimation of the individual rate constants.

Initial estimation of k_2 and k_4

Solving the definition equation of the turnover number $\frac{V_{\max}}{R^*} = \frac{k_2 k_4}{(k_2 + k_4)}$ = 594 s^{-1} for k_2 and k_4, respectively, yields:

$$k_2 = \frac{k_4 \, 594 s^{-1}}{k_4 - 594 s^{-1}} \qquad \text{(S1)}$$

and

$$k_4 = \frac{k_2 \, 594 s^{-1}}{k_2 - 594 s^{-1}} \qquad \text{(S2)}$$

The lower limit for both values is thus $k_2 > 594$ s^{-1} and $k_4 > 594$ s^{-1}. Importantly, the two values are mutually dependent (Eq. S1 and S2).

Initial estimation of k_1

The lower limit for k_1 (set B in Table S4) is given by (see (2) for details):

$$k_1 \geq \frac{k_{cat}}{K_m^G} = \frac{V_{\max}}{R^* K_m^G} = \frac{k_1 k_2}{(k_{-1} + k_2)} = 0.272 \ \mu m^2 \, s^{-1} \qquad \text{(S3)}$$

The upper limit of k_1 is estimated as follows:
With the definition of K_d^G, k_{-1} can be substituted in Eq. (S3) by $k_{-1} = k_1$ 534 μm^{-2}, yielding after solving for k_1:

$$k_1 = \frac{0.272 \mu m^2 s^{-1} \cdot k_2}{(k_2 - 145 \ s^{-1})} \qquad \text{(S4)}$$

With $k_2 > 594$ s^{-1} (see above) one obtains $k_1 < 0.36$ $\mu m^2 s^{-1}$ (set A in Table S4)

Initial estimation of k_{-1}

Solving the definition of $K_d^G = \frac{k_{-1}}{k_1} = 534 \mu m^{-2}$ for k_{-1} yields

$k_{-1} = k_1$ 534 μm^{-2} (S5)

With the limiting values for k_1 one obtains

$145\ s^{-1} < k_{-1} < 192\ s^{-1}$.

Initial estimation of k_{-2}

Solving the definition of $K_d^{GDP} = \frac{k_2}{k_{-2}} = 274\,\mu M$ for k_{-2} yields

$$k_{-2} = \frac{k_2}{274\,\mu M} \qquad \text{(S6)}$$

With $k_2 > 594\ s^{-1}$ one obtains

$k_{-2} > 2.2\ \mu M^{-1}\ s^{-1}$

Initial estimation of k_3

Analogous to the estimation of the lower limit for k_1 (see above), the lower limit for k_3 is given by:

$$k_3 \geq \frac{k_{cat}}{K_m^{GTP}} = \frac{V_{\max}}{R^* K_m^{GTP}} = 2.57\,\mu M^{-1}\,s^{-1}$$

Initial estimation of k_{-3}

A limiting value for k_{-3} can be obtained from the fact, that the Michaelis constant for GTP (K_m^{GTP}) confine the upper limit of the dissociation constant for GTP (K_d^{GTP}):

$$K_d^{GTP} = \frac{k_{-3}}{k_3} \leq K_m^{GTP} \qquad \text{(S7)}$$

Solving Eq. S7 for k_{-3} yields

$$k_{-3} \leq K_m^{GTP}\ k_3$$

and with $k_3 > 2.57\ \mu M^{-1}\ s^{-1}$ and $K_m^{GTP} = 231\ \mu M$ one obtains

$k_{-3} < 594\ s^{-1}$

Estimation of k_{-4}, k_{sol} and k_{-sol}

Dissociation of G* from R* is in the visual system followed by dissociation of G* into its subunits (GαGTP and Gβγ) and a subsequent quantitative dissociation of GαGTP from the membranes. Since the overall reaction is essentially irreversible under the experimental conditions used (2), the respective rate constants were set as given in Table S4.

Estimation of k_{M2} and k_{-M2}

Values of k_{M2} and k_{-M2} were calculated for 22°C and pH 7.4 with the equations provided by (5). The resulting values (see Table S4) are consistent with published values obtained at 20°C, pH 7.0 and pH 8.0 (6) and allow to calculate the fraction of active receptor relative to the total amount of light-activated rhodopsin (f^A; see (2)):

$$f^A = \frac{k_{M2}}{(k_{M2} + k_{-M2})} = 0.71$$

Estimation of rate constants by ODE fitting

The classic G-protein activation scheme depicted in Fig. 1A (reactions 1-3) was used to derive a system of ordinary differential equations (ODE):

$$[M1]_n' = - k_{M2}[M1]_n + k_{-M2}[R^*]_n$$

$$[R^*]_n' = k_{M2}[M1]_n - k_{-M2}[R^*]_n - k_1[R^*]_n[G]_n + k_{-1}[R^*G]_n + k_4[R^*G^*]_n - k_{-4}[R^*]_n[G^*]_n$$

$$[G]_n' = - k_1[R^*]_n[G]_n + k_{-1}[R^*G]_n$$

$$[R^*G]_n' = k_1[R^*]_n[G]_n - k_{-1}[R^*G]_n - k_2[R^*G]_n + k_{-2}[GDP][R^*G_0]_n$$

$$[R^*G_0]_n' = k_2[R^*G]_n - k_{-2}[GDP][R^*G_0]_n - k_3[GTP][R^*G_0]_n + k_{-3}[R^*G^*]_n$$

$$[R^*G^*]_n' = k_3[GTP][R^*G_0]_n - k_{-3}[R^*G^*]_n - k_4[R^*G^*]_n + k_{-4}[R^*]_n[G^*]_n$$

$$[G^*]_n' = k_4[R^*G^*]_n - k_{-4}[R^*]_n[G^*]_n - k_{sol}[G^*]_n + k_{-sol}[G^*_{sol}]_n$$

$$[G^*_{sol}]_n' = k_{sol}[G^*]_n + k_{-sol}[G^*_{sol}]_n$$

where the subscript of the variables (n = 1-7) identifies the individual dissociation signal used in this study. All protein concentrations are given in numbers/μm^2, and [GDP] and [GTP] denote the volume concentrations of the respective nucleotide. Due to the different concentration units, [GTP] and [GDP] are treated in the following as constants.

In order to estimate the individual rate constants, data points of seven dissociation signals were simultaneously fitted with the ODE model by applying a multiple least squares fit procedure, *i.e.* the simultaneous fit of $[G^*_{sol}]_n$ using one and the same set of rate constants. Representative dissociation signals were taken from a previous study and scaled to concentration units as described (2). The initial (t = 0) concentrations are summarized in Table S2.

In the fit procedure (Scientist Software, MicroMath), rate constants k_{-4}, k_{sol}, k_{-sol}, k_{M1} and k_{-M1}, respectively, were fixed to the values shown in Table S4. In order to include the constrains

given by the experimentally determined kinetic constants V_{max}/R^*, K_m^G, K_m^{GTP}, K_d^G and K_d^{GDP} (Table S1), the rate constants k_{-1}, k_{-2}, k_3 and k_4, respectively, were incorporated in the fit procedure by the following equations:

$k_{-1} = k_1\ 534\ \mu m^{-2}$ (see Eq. S5)

$$k_{-2} = \frac{k_2}{274\mu M}$$ (see Eq. S6)

$$k_4 = \frac{k_2\ 594 s^{-1}}{k_2 - 594 s^{-1}}$$ (see Eq. S2)

Solving the definition of K_m^{GTP} = 231 µM (Table S1) for k_3 yields

$$k_3 = \frac{k_2(k_{-3} + k_4)}{231\mu M(k_2 + k_4)}$$

The two sets of rate constants (Table S4) were then obtained by ODE-fitting with k_1 fixed either to its upper limit (k_1 = 0.36 $\mu m^2 s^{-1}$, set A in Table S4) or to its lower limit (k_1 = 0.27 $\mu m^2 s^{-1}$, set B in Table S4). In both cases the rate constants k_2 and k_{-3} were allowed to vary within the limits described above. Both sets of rate constants fitted the experimental data equally well (Fig. 2 A).

In order to verify the results, another series of dissociation signals measured in the presence of 200 µM GTP (0 µM GDP, data taken from (2)) were simulated with both sets of rate constants. As seen in Fig. 2 B, the resulting traces are in good agreement with the experimental data.

Since the rate of GDP uptake by the R*G complex (i.e. rate constant k_{-2}) is not defined in the absence of GDP, the value of k_{-2} was subsequently estimated by applying the ODE fitting procedure to dissociation signals measured in the presence of 750 µM GDP and 2000 µM GDP (data taken from (2)). In this case k_{-2} was allowed to vary while all other rate constants were fixed to the values given in Table S4. The results are depicted in Fig. S1 and summarized in Table S5.

Table S5: Validation of k_{-2}

	750 µM GDP	2000 µM GDP
Set A	k_{-2} = 2.4 $\mu M^{-1}s^{-1}$	k_{-2} = 2.7 $\mu M^{-1}s^{-1}$
Set B	k_{-2} = 240 $\mu M^{-1}s^{-1}$	k_{-2} = 270 $\mu M^{-1}s^{-1}$

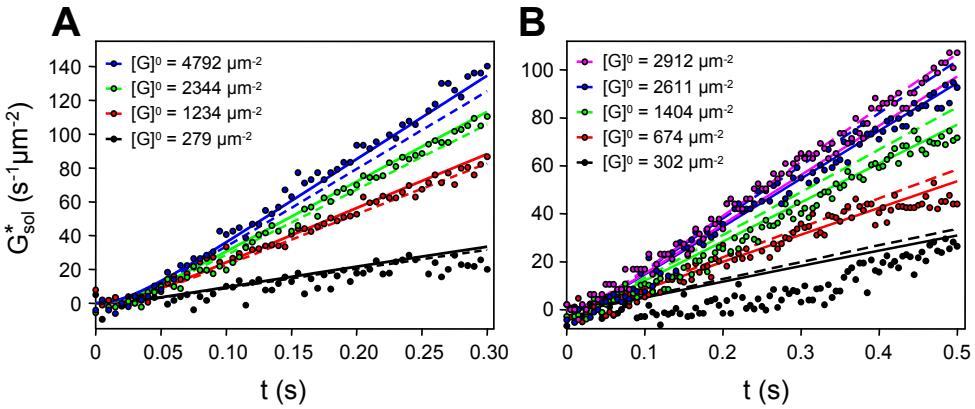

Fig. S1 ODE-fitting of k_{-2}. ODE-fits (lines) with k_{-2} as open parameter to representative dissociation signals (circles; taken from (2)) measured with 200 µM GTP, and 750 µM GDP (**A**) or 2000 µM GDP (**B**). **(A)** Best fits (solid lines) yield k_{-2} = 2.4 µM^{-1}s^{-1} (rate constant set A, Table S4) or k_{-2} = 240 µM^{-1}s^{-1} (rate constant set B). (**B**) Best fits (solid lines) yield k_{-2} = 2.7 µM^{-1}s^{-1} (rate constant set A) or k_{-2} = 270 µM^{-1}s^{-1} (rate constant set B). Dotted lines represent simulations with rate constant set A and k_{-2} = 2.7 µM^{-1}s^{-1} (A) or k_{-2} = 2.4 µM^{-1}s^{-1} (B).

Pre-complex case

In the case of nonproductive complex formation between inactive receptor (R) and Gt (reaction (4) in Fig. 1A; pre-complex case), the ODE model was extended as follows:

$$
\begin{aligned}
[\text{Meta1}]_n' &= -k_{M2}[\text{Meta1}]_n + k_{-M2}[R^*]_n \\
[R^*]_n' &= k_{M2}[\text{MetaI}]_n - k_{-M2}[R^*]_n - k_1[R^*]_n[G]_n + k_{-1}[R^*G]_n + k_4[R^*G^*]_n \\
&\quad - k_{-4}[R^*]_n[G^*]_n \\
[G]_n' &= -k_1[R^*]_n[G]_n + k_{-1}[R^*G]_n - k_{pre}[R]_n[G]_n + k_{-pre}[RG]_n \\
[R^*G]_n' &= k_1[R^*]_n[G]_n - k_{-1}[R^*G]_n - k_2[R^*G]_n + k_{-2}[GDP][R^*G_0]_n \\
[R^*G_0]_n' &= k_2[R^*G]_n - k_{-2}[GDP][R^*G_0]_n - k_3[GTP][R^*G_0]_n + k_{-3}[R^*G^*]_n \\
[R^*G^*]_n' &= k_3[GTP][R^*G_0]_n - k_{-3}[R^*G^*]_n - k_4[R^*G^*]_n + k_{-4}[R^*]_n[G^*]_n \\
[G^*]_n' &= k_4[R^*G^*]_n - k_{-4}[R^*]_n[G^*]_n - k_{sol}[G^*]_n + k_{-sol}[G^*_{sol}]_n \\
[G^*_{sol}]_n' &= k_{sol}[G^*]_n + k_{-sol}[G^*_{sol}]_n \\
[R]' &= -k_{pre}[R]_n[G]_n + k_{-pre}[RG]_n \\
[RG]' &= k_{pre}[R]_n[G]_n - k_{-pre}[RG]_n
\end{aligned}
$$

Since the amount of RG-complex (and thus depletion of free Gt) depends on the values of k_{pre} and k_{-pre}, calculation of the initial concentrations of RG ($[RG]_n^{0\,pre}$), G ($[G]_n^{0\,pre}$) and R ($[R]_n^{0\,pre}$) were integrated in the fit procedure:

$$[RG]_n^{0\,pre} = \frac{\left(K_d^{pre} + [R]_n^0 + [G]_n^0\right) - \sqrt{\left(K_d^{pre} + [R]_n^0 + [G]_n^0\right)^2 - 4[R]_n^0[G]_n^0}}{2}$$

$$[G]_n^{0\,pre} = [G]_n^0 - [RG]_n^{0\,pre}$$

$$[R]_n^{0\,pre} = [R]_n^0 - [RG]_n^{0\,pre}$$

were $K_d^{pre} = \frac{k_{-pre}}{k_{pre}}$ (i.e. dissociation constant of the RG-complex), $[R]_n^0$ = 25000 µm^{-2} and $[G]_n^0$ as given in Table S2.

In order to obtain the limiting case, values of k_{pre} and k_1 were set to the diffusion limit. To compute this, we rely on the Smoluchowski-Equation:

$$k_1^{max} = 4\pi(D_R + D_G)(r_{r,R} + r_{r,G}).$$

See Table 2 for the values of the used diffusion constants and reaction radii. We obtain k_1^{max}=0.12µm^3/s. This second order rate constant can be transformed from its volume concentration to the surface concentration necessary for our needs by the formula of (2):

$$\frac{[X]^{3D}}{[X]^{2D}} = \frac{[R]^{3D}}{[R]^{2D}}.$$

Experiments were conducted at $[R]^{3D}$ = 3µM and $[R]^{2D}$ = 25,000 µm^{-2}. Thus we obtain k_1^{max} = 1.67 µm^2/s.

Rates k_{pre} and k_1 were both set to k_1^{max} and k_{-pre} was allowed to vary in the ODE model (all other rate constants were fixed to the values given in Table S4, Set A). The resulting fit yields the lower limit of k_{-pre} (k_{-pre} > 11200 s^{-1}). Under these conditions and with native Gt concentrations (2500 - 3000 Gt µm^{-2}), about 80 % of total Gt would be initially bound to inactive receptors.

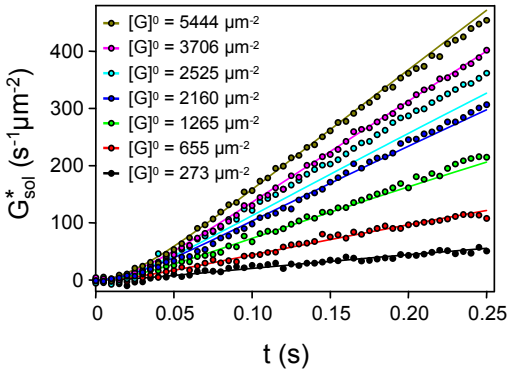

Fig. S2 ODE-fitting of k_{-pre}. ODE-fits (solid lines) with k_{-pre} as open parameter to dissociation signals (circles; measuring conditions as in Tables 1 and S2; rate constants as in Table S4). For details see text.

Model Geometry

In the reference experiment (2), disk membranes expanded to roughly spherical vesicles after having been extracted from the rod outer segment. Thus, we confine particle diffusion to a spherical surface by applying a harmonic potential along the surface normal (see Supporting Information for details). Simulating vesicle sizes found in experiment (r = 220 nm, A = 0.6 μm^2) is very CPU-intensive. Therefore, the size of the simulated vesicles was chosen such that it would host one R* on average (radius r = 120nm and surface area A = 0.18 μm^2). To mimic physiological conditions, the simulated particles comprise one R*, 4,500 R and 450 G. (See Figure 3 B for depiction).

Partice Radius Parametrization

All molecules involved in the system fall in three categories: R-type, G-type and RG-type. The R-type comprises hodopsin (R) in its inactive Meta I form (M1) and its active Meta II form (R*). The G-type contains G-proteins in its inactive (G) and active (G*) forms and the RG-type spans over all complexes formed from R-type and G-type molecules. Based on the two dimensional (2D) surface geometry of the system, all molecules are modeled as 2D disk objects. These particles collide with each other if they get closer than the sum of their collision radii (r_c). Similarly, if the distance between reacting particles is smaller than the sum of their reaction radii (r_r), a reaction can happen. In order to parametrize these radii, we rely on crystal structures (R: bovine, 1U19 (7), R*: bovine 3PQR (8); G: bovine, 1GOT (9), RG: 3SN6 (10))

Rhodopsin is a transmembrane protein, approximated by a disk with collision and reaction radii $r_c = r_r = 2.1$ nm. Note that collisions are not handled by hard space exclusions, but rather by a soft-core interaction, therefore $r_c = r_r$ does represent a nonzero reaction volume.

G is bound to disk membranes by two small lipid membrane anchors. The soluble part of the protein is modeled disk shaped with radius $r_c = 3.4$ nm, enclosing the same area as the elliptical shape of G in the crystal with axe diameters of 9 nm x 5 nm. This is the radius with which G proteins will collide with each other. R, on the other hand, can move beneath G, only colliding with the membrane anchors of G. We therefore consider two types of collision radii: $r_{c,mb}$ for membrane internal collisions and $r_{c,sol}$ for the collisions of the soluble part. The two lipid moieties form one membrane anchor with a footprint of 73 nm^2 inside the membrane (11), resulting in a collision radius of $r_{c,mb} = 0.6$ nm in our model. The reaction radius of G ($r_{r,G}$) is chosen based on the distance of the N-terminal helix in G_α to the membrane anchors (5.2 nm - 5.5 nm). The anchor and some helix residues are missing in the crystal structure that would enlarge these distances. For these reasons, we set the reaction radius conservatively to $r_{r,G} = 3$ nm (assuming a 6nm distance between anchor and N-terminal helix).

For the RG-type, we use $r_{c,RG,mb} = 2.1$ nm, i.e. radius of rhodopsin, and $r_{c,RG,sol} = 3.4$ nm, i.e. radius of soluble part of G. RG-complexes do not participate in reactions with other particles and therefore possess no reaction radius. See Fig. 2 for an illustration of the particle model and Table 2 for a summary of the data.

Particle collisions:

During simulation, repulsive particle-particle interaction potentials prevent overlaps between particles. The stiffness of these potentials is related to the timestep with which the dynamics

can be discretized. Too large timesteps in a given potential lead to large discretization errors in the time integration of the equations of motion. There is a trade-off between stiff potentials that prevent particles from overlapping and large timesteps needed to reach biologically relevant timescales. Here, we use harmonic softcore potentials:

$$\mathrm{U(r)} = \begin{cases} 0.5\ \mathrm{k_{pot}}(\mathrm{r} - \mathrm{r_0})^2 & \text{if } \mathrm{r} < \mathrm{r_0} \\ 0 & \text{else} \end{cases}, \tag{S 8}$$

with distance r between two particles, collision distance r_0 and k_{pot} = 10 kJ/mol/nm^2. The resulting repulsion potentials have a small overlap region of around 0.8*nm* between full space exclusion and no interaction, resembling the fact, that biomolecules are not solid objects and feature certain long range interactions. See the following section for details about potential Parametrization.

Potential Parametrization

The used softcore potentials allow a small overlap between particles. Therefore, in order to correctly model the desired molecular radii, we have to adjust the force constant of the repulsive term of the potential in order to arrive at a distance distribution that matches our expected particle sizes. Given the potential, we can calculate the residence probability $p(r)$ of particles in a certain distance r to one another with the following equation:

$$p(r) = 4\pi r^2 e^{\left(-\frac{U(r)}{k_B T}\right)}. \tag{S 9}$$

We define the inner core radius r_c of a particle as the region below the 25% threshold of $p(r)$, $r_c = \{r \mid p(r) = 0.25\}$ (See Figure S1). In order to set r_c to the desired particle radii given in Table 2, we have to input slightly larger radii: $r_c^{in} = r_c + 0.4nm$.
Figure S1 displays the repulsion potential in Eq. S8 for the collision distances of R-R, R-G and G-G, together with the residence probability $p(r)$ (Eq. S9) for these distances. See also Ref. (12) for details about potential parametrization.

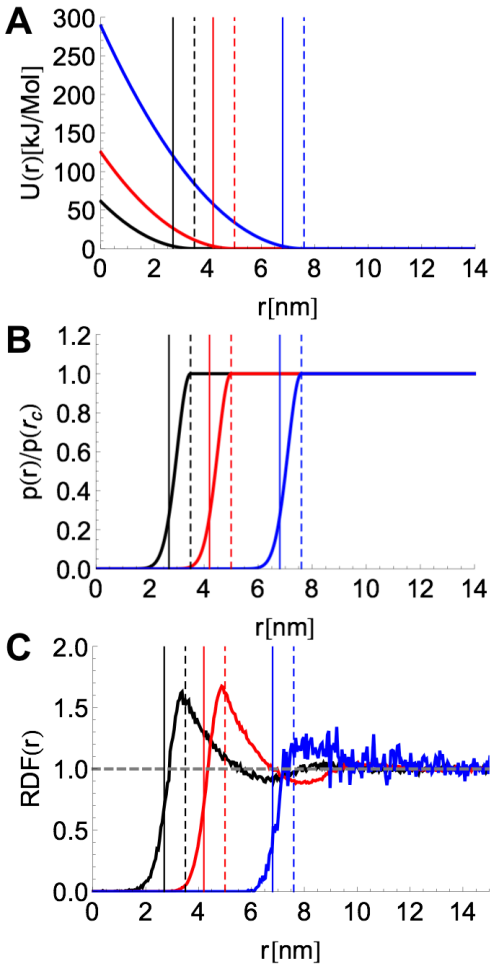

Figure S3: Input and resulting collision distances between particles. Collision distances are investigated for the following pairings: R-G (black), R-R (red) and G-G (blue). Input radii (solid vertical lines) and resulting collision radii (dashed vertical lines) are displayed in the same color code. R-G: $r_{c,R,mb}^{in}$+$r_{c,G,mb}^{in}$ = 3.5nm, $r_{c,G,mb}$ = 2.7nm; R-R: $r_{c,R,mb}^{in}$+$r_{c,R,mb}^{in}$ = 5.0nm, $r_{c,R,mb}$+$r_{c,G,mb}$ = 4.2nm; G-G: $r_{c,G,sol}^{in}$+$r_{c,G,sol}^{in}$ = 7.6nm, $r_{c,R,mb}$+$r_{c,RGmb}$ = 6.8nm. **A:** Potential governing particle interactions (Eq. S8). **B:** Residence probability of particles, calculated from Eq. S9. **C:** Radial distribution function (rdf) calculated from Monte Carlo simulation of the full sample simulation including 4500 R and 450 G particles. Depicted are averages of 100 rdfs.

Timestep Derivation

The time step was derived as described in Schöneberg and Noé 2013 (12): The size of Δt depends on the stiffness of the used potentials. In case of the current disk vesicle model, there are two potentials. A harmonic particle repulsion potential responsible for particle overlap prevention and a harmonic spherical shaped geometry potential keeping the particles on a spherical surface during the simulation. See SI Figure 2 for a depiction of the radial distribution function (RDF) of both potentials (upper left: particle repulsion, lower left: vesicle geometry). First a Monte Carlo simulation was performed in order to obtain an RDF that is not affected by time step discretization errors. This standard was then compared to BD-Simulation results of different Δt. The root mean squared error of the differences between standard and BD-simulation was computed and the largest Δt chosen that still lead to reasonable results.

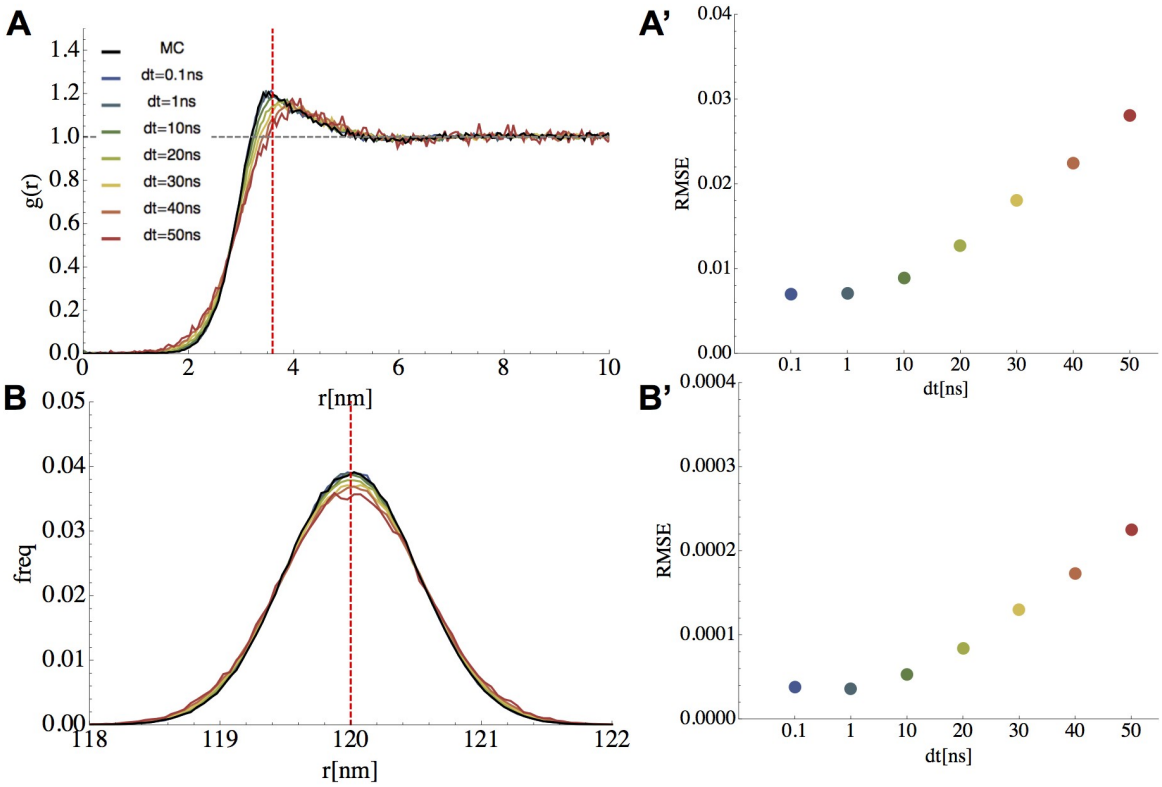

Figure S4: Influence of timestep choice on discretization error. Radial distribution function (rdf) of the two types of potentials is depicted that exist in the simulation: the pairwise repulsion potential (A) and the spherical geometry potential (B) holding the particles at 120nm distance to the origin. The black line indicates MCMC simulations that do not involve time discretization errors. The colored lines depict integration timestep length for the Brownian particle dynamics. Depicted are averages from 6 simulations per scenario. A' and B' depict the root mean squared error of the rdf results in MCMC compared with the respective time discretized Brownian particle dynamics.

Diffusion Constant Parametrization

Diffusion is a phenomenological process of large particles that perform a random motion when immersed in a solvent. Its magnitude is measured by the diffusion constant D. The Stokes-Einstein-Equation relates D to temperature T, solvent viscosity η and the radius of the immersed particle r_c, weighted by the Boltzmann-constant k_B:

$$D = \frac{k_B T}{6\pi\,\eta\,r_c}. \qquad (S10)$$

The presences of other particles may slow down the effective diffusion speed, an effect usually referred to as crowding. In monitoring the mean square displacements ($\mathrm{msd(t)} = \langle (x_0 - x_t)^2 \rangle$) of the particles the diffusion constant can be obtained as follows:

$$D = \frac{1}{2d}\,\frac{\mathrm{d}\,\langle (x_0 - x_t)^2 \rangle}{\mathrm{d}\,t}. \qquad (S11)$$

D is proportional to the slope of the msd with d being the dimensionality of the diffusion process ($d = 2$ in this case). In crowded systems a biphasic behavior can be observed. In the first few timesteps, particles move along their mean free path with the microscopic diffusion constant D_{micro}. On longer timescales, particles collide with each other. This crowding slows down the average movement, resulting in a smaller apparent diffusion constant $D \leq D_0$.
D_0 can be derived via Eq. S10 using $\eta = 100\ cP$ at $22°C$ (13) as an estimate for the viscosity of the disk membrane. (Note that this viscosity value is assumed to be the viscosity of the lipid membrane only. Using a viscosity of a disk membrane including all proteins, Eq. S10 would result in D.) While R has a rather well-defined radius in the membrane resulting in $D_{micro}^{R,theory} = 1\mu m^2 s^{-1}$, the situation is less clear for G which has a small membrane anchor that would diffuse fast on its own ($D_0^{G,anchor,theory} = 3.6\mu m^2 s^{-1}$) but a large soluble domain whose footprint size would give rise to a much slower diffusion of ($D_0^{G,sol,theory} = 0.6\mu m^2 s^{-1}$) in the membrane. The latter value is most likely strongly underestimated, as the soluble domain is mostly affected by much less viscous cytoplasm.
Depending on the experimental method used, either D_0 or D is measured. The observed value range of D of rhodopsin is [D^R = 0.13 μm^2/s - 0.73 μm^2/s] (14-19), being measured in physiological systems at 22°C, mostly in amphibian rod cells and based on fluorescence recovery after photobleaching (FRAP) experiments. The value for G protein ($D^G = 1.2$ μm^{2}s^{-1}) is based on an estimate of the diffusion of similar proteins and is also considered a D_{macro} value (see Ref. (20) for a review of the experiments for R and the estimate for G).
High values of D are likely to cancel any geometric effects of rhodopsin architecture while low values of D would point out geometrical effects more prominently. To do the most fair comparison between experimentally found structures, considering their ability to reproduce experimentally measured kinetics, we chose the upper limit of the available diffusion constants.
If we assume that all proteins are explicitely resolved in our simulation, given the number of particles, their macroscopic diffusion constants D and their microscopic arrangement (i.e. free diffusion of all particles, fractions of immobile particles e.g. racks of rhodopsin dimers, etc), D_0 values can be sampled by simulation that reproduce D under the given conditions on long timescales (See Figure S5 and Ref (12)).

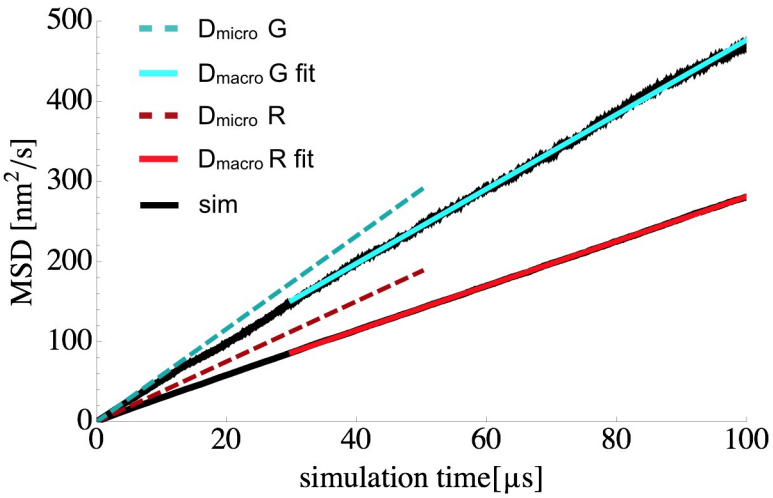

Figure S5. Parametrization of Microscopic Diffusion Constant by Simulation. The mean squared displacement (MSD) over time is depicted for R (red fits above black simulation data) and G-protein (G, blue fits above black simulation data) in the standard disc vesicle simulation. During the first timesteps, particles diffuse with D_{micro} (dashed lines). On longer time-scales, crowding slows down the particle movement (solid lines) to D_{macro}. Depicted are averages from 6 simulations.

Conversion of Reaction Rates into Reaction Probabilities

Due to time discretization in ReaDDy, all unimolecular reaction rates have to be converted in probabilities, that the reaction has happened within each timestep, provided that the requirements for a reaction are met. There are no requirements for unimolecular reactions. For bimolecular reactions, the educt particle distance has to be closer than the sum of the educt reaction radii. Rates of unimolecular reactions represent microscopic reaction rates, for bimolecular reactions, these have first to bextracted from macroscopic bimolecular rates (see next section). The reaction probability is obtained from the Poisson probability of finding at least one reaction event with rate k^{micro} in a time window Δt (12):

$$p(\Delta t) = 1 - \exp\left(k^{micro} \ \Delta t \right) \qquad \text{(S 12)}$$

Microscopic Rate Constant Parametrization for Bimolecular Reactions

Bimolecular reactions, e.g. the initial R*G complex formation

$$R^* + G \underset{k_{-1}}{\overset{k_1}{\rightleftharpoons}} R^*G, \qquad \text{(first reaction in Eq. 2)}$$

require a modeling step for microscopic simulations. A bimolecular reaction rate in an ODE model includes both the bimolecular rate at which the two particles form an encounter complex by diffusion k_{enc} and the unimolecular rate at which this complex overcomes the activation energy k^{micro}:

$$R^* + G \underset{k_{-enc}^{R^*G}}{\overset{k_{enc}^{R^*G}}{\rightleftharpoons}} R^* \cdot G \underset{k_{-1}}{\overset{k_1^{micro}}{\rightleftharpoons}} R^*G. \qquad (2.2)$$

In our simulations, diffusion is modeled explicitly. I. e. particles have to come closer than the sum of their reaction radii r_r in order to attempt a reaction with rate k_1^{micro}. In order to parametrize the simulation to the macroscopic reaction rate k_1, we must search a value for k_1^{micro} that, in conjunction with particle concentration, diffusion constants and reaction radii, leads to the effective rate k_1.

For three-dimensional diffusion, an explicit formulate exists to compute k_1^{micro} (21). For the present two-dimensional system we have to rely on sampling. k_1^{micro} is the only free parameter in the free diffusion case, and can therefore obtained by sampling G protein activation in this geometry, using the parameters from Table 1 and Table 2. The value $k_{micro} = 5000s^{-1}$ matched best the production rate of 285 G_{sol}^*/s/R*, the initial catalysis rate of the ODE model starting with R* (instead of with M1). See Figure 4 for a depiction of the sampling results.

This procedure is only possible for the scenarios that contain a single bimolecular reaction. In the precomplex scenario, the RG complex formation reaction introduces a second microscopic reaction rate k_{pre}^{micro} (Eq. 4.2 in Figure 1), which renders the system indeterminate.

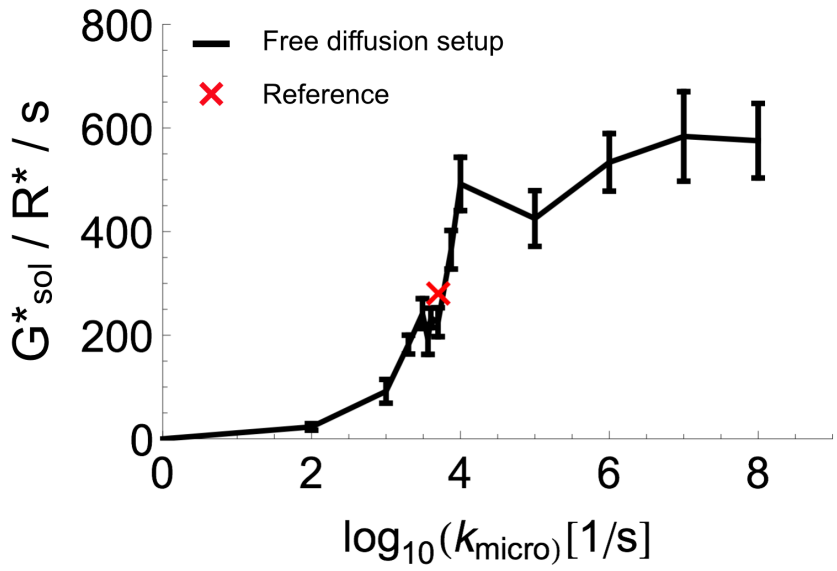

Figure S6 Parametrization of the microscopic R*+G association rate: k_1^{micro} is the single microscopic rate in the cascade that arises from a macroscopic bimolecular reaction (R* + G → R*G) in the free diffusion scenario. It is parametrized by sampling, using the standard disk vesicle geometry including reactions. The red cross indicates the number of produced G* in the experiment at [G] = 2500/μm^2, starting initially with R* . The plateau at large values of k_1^{micro} indicates, that in these regions, the system is no longer limited by the activation-complex reaction. Other steps in the reaction cascade are now rate-limiting. Depiced are averages and standard errors of 6 simulations per k_1^{micro}.

Time shifting method to simulate first M1 → R* **transition**

Instead of starting the simulation with an active receptor in Meta1 form, each trajectory is started in Meta2 form (R*) that capable of activating G. The shift in time, when this initial transition from Meta1 to Meta2 has happened is simulated a posteriori: For each trajectory, an ensemble of 1000 reaction times is drawn according to probability distribution $p(t) = 1 - exp(-k_{M2}t)$. Trajectories are shifted in time and averaged.

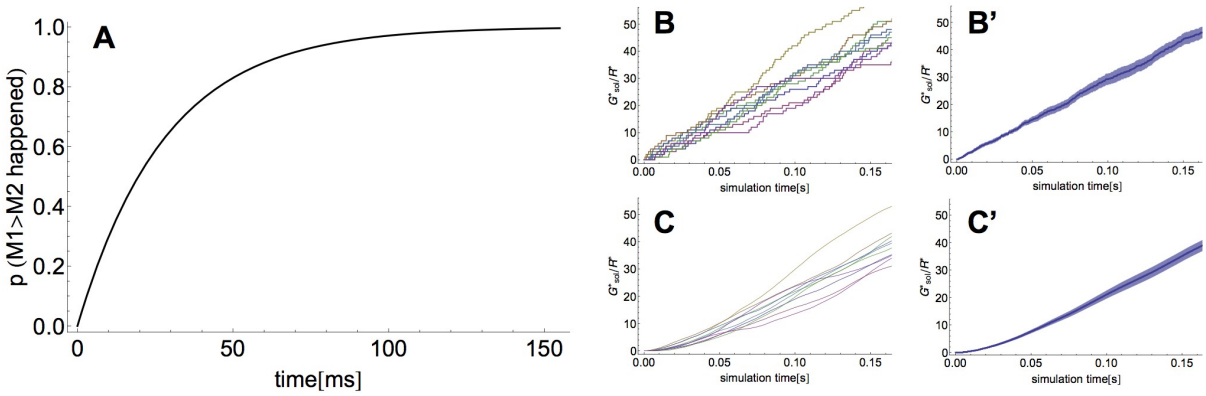

Figure S7 Time shifting method to simulate first M1 → R* transition: A: Given the time that has passed, what is the probability, that M1 has switched its state to R*. **B**: Raw G^*_{sol} production traces from simulation and their average (B'). **C**: Each raw trace, 1000 times time shifted and averaged. **C'**: Average of C.

Rack geometry structure derivation

The geometry for the rack case simulation was derived using image analysis of the microscopic image published by Fotiadis et al. 2003 (22). Rack structures that could be recognized on the image free of doubt were overlayed with lines that had the thickness of an R-dimer (Figure S8 A). The size distribution of these lines was recorded and discretized (Figure S8 B). The resulting histogram of Rack lengths was fitted with an exponential distribution, resulting a distribution of rack lengths *l*:

$$p_l \approx 0.261 \exp(-0.261\, l\,)$$

Thus, rack sizes were generated according to the following formula:

$$\mathrm{n}_l = \left\lfloor \frac{N}{2} p_l \right\rfloor,$$

where N is the total number of R molecules and the brackets denote rounding to the next-lower integer. For the fit, the counts for rack size 0 and 1 (i.e. individual Rs and dimers) were omitted because they could not be assigned on the image free of doubt.

Using this distribution, geometries were created, based on our assumed native conditions (Table 1). 80% of the available R was assigned to racks and 20% of the available R to be monomeric and freely diffusing. R* is once considered as monomeric and once as part of a rack. See a depiction of the resulting geometries in Fig S8 C.

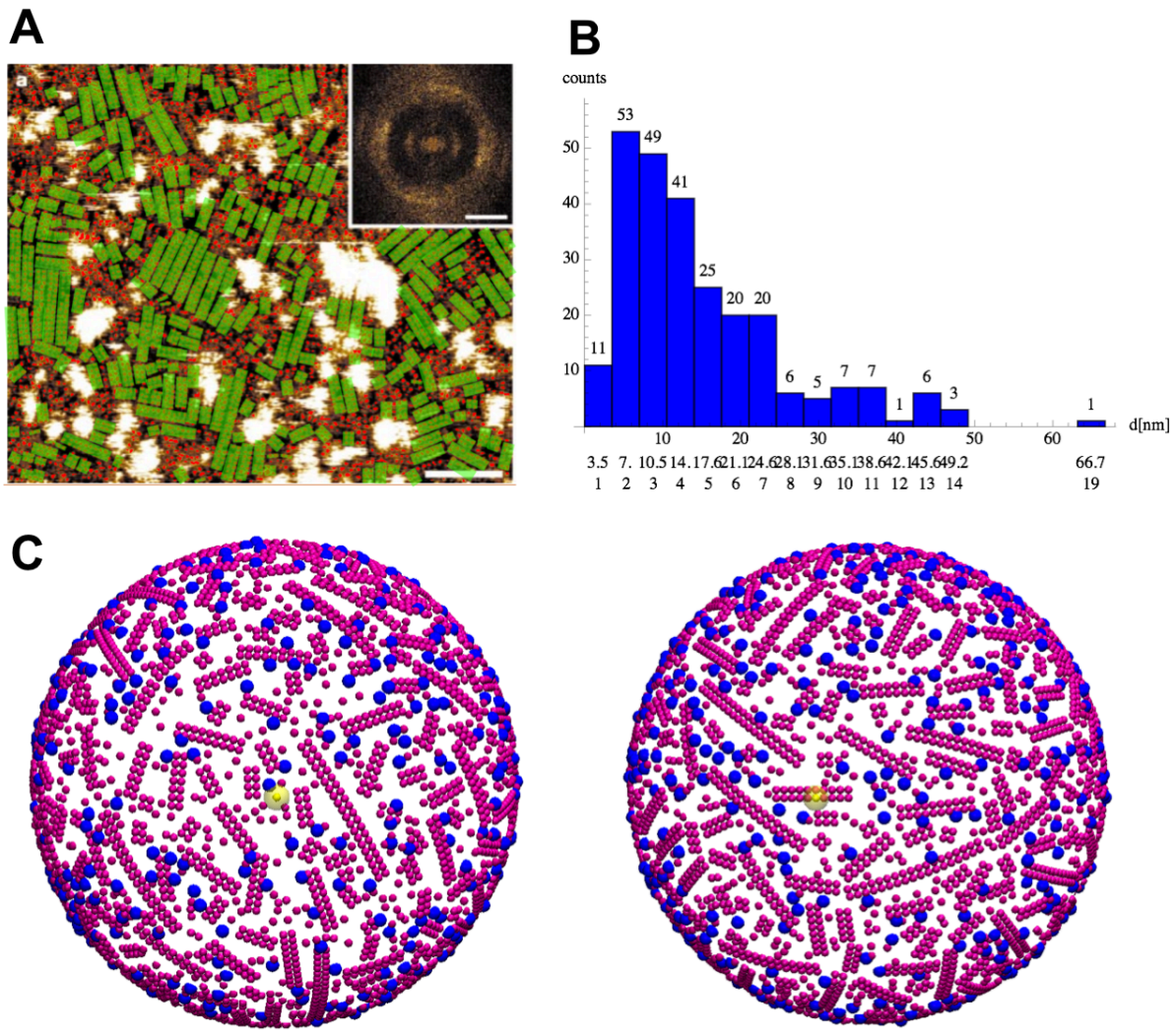

FIGURE S8: Derivation of rack size distribution by image analysis and resulting geometry (*A*) Microscopic image from Fotiadis et al., Nature 2003. Adapted by permission from Macmillan Publishers Ltd: Fotiadis et al, Nature. 421: 127–128, copyright 2003. (22), overlayed with markers for racks that could be identified individually (*green*). (*B*) Histogram of the rack size distribution in A, based on the identified racks. (*C*) Resulting geometries from the rack distribution on a disk vesicle with parameters as given in Table 1. R* is depicted once as monomeric (*left*) and once as part of a rack (*right*). Note, that the density in our models is 25,000 R μm^{-2}, as opposed to 50,000 R μm^{-2} in (22).

Supporting References

1. Segel, I.H. 1975. Enzyme Kinetics. John Wiley & Sons, Inc.

2. Heck, M., and K.P. Hofmann. 2001. Maximal rate and nucleotide dependence of rhodopsin-catalyzed transducin activation - Initial rate analysis based on a double displacement mechanism. Journal of Biological Chemistry. 276: 10000–10009.

3. Kühn, H., N. Bennett, M. Michel-Villaz, and M. Chabre. 1981. Interactions between photoexcited rhodopsin and GTP-binding protein: kinetic and stoichiometric analyses from light-scattering changes. Proc. Natl. Acad. Sci. USA. 78: 6873–6877.

4. Heck, M., A. Pulvermüller, and K.P. Hofmann. 2000. Light scattering methods to monitor interactions between rhodopsin-containing membranes and soluble proteins. Meth. Enzymol. 315: 329–347.

5. Parkes, J.H., and P.A. Liebman. 1984. Temperature and pH dependence of the metarhodopsin I-metarhodopsin II kinetics and equilibria in bovine rod disk membrane suspensions. Biochemistry. 23: 5054–5061.

6. Jäger, S., I. Szundi, J.W. Lewis, T.L. Mah, and D.S. Kliger. 1998. Effects of pH on rhodopsin photointermediates from lumirhodopsin to metarhodopsin II. Biochemistry. 37: 6998–7005.

7. Okada, T., M. Sugihara, A.-N. Bondar, M. Elstner, P. Entel, et al. 2004. The Retinal Conformation and its Environment in Rhodopsin in Light of a New 2.2Å Crystal Structure. J.Mol.Biol. 342: 571–583.

8. Choe, H.-W., Y.J. Kim, J.H. Park, T. Morizumi, E.F. Pai, et al. 2012. Crystal structure of metarhodopsin II. Nature. 471: 651–655.

9. Lambright, D.G., J. Sondek, A. Bohm, N.P. Skiba, H.E. Hamm, et al. 1996. The 2.0 A crystal structure of a heterotrimeric G protein. Nature. 379: 311–320.

10. Rasmussen, S.G.F., B.T. DeVree, Y. Zou, A.C. Kruse, K.Y. Chung, et al. 2012. Crystal structure of the b. Nature. 477: 549–555.

11. Seitz, H.R., M. Heck, K.P. Hofmann, T. Alt, J. Pellaud, et al. 1999. Molecular Determinants of the Reversible Membrane Anchorage of the G-Protein Transducin. Biochemistry. 38: 7950–7960.

12. Schöneberg, J., and F. Noé. 2013. ReaDDy - A Software for Particle-Based Reaction-Diffusion Dynamics in Crowded Cellular Environments. PloS One. 8: e74261.

13. Kung, C., and J. Reed. 1986. Microviscosity Measurements of Phospholipid Bilayers Using Fluorescent Dyes That Undergo Torsional Relaxation. Biochemistry. 25: 6114–6121.

14. Liebman, P., and G. Entine. 1974. Lateral Diffusion of Visual Pigment in Photoreceptor Disk Membranes. Science. 185: 457–459.

15. Takezoe, H., and H. Yu. 1981. Lateral diffusion of photopigments in photoreceptor disk membrane vesicles by the dynamic Kerr effect. Biochemistry. 20: 5275–5281.

16. Gupta, B., and T. Williams. 1990. Lateral diffusion of visual pigments in toad (Bufo marinus) rods and in catfish (Ictalurus punctatus) cones. The Journal of Physiology.

17. Wang, Q., X. Zhang, L. Zhang, F. He, G. Zhang, et al. 2008. Activation-dependent Hindrance of Photoreceptor G Protein Diffusion by Lipid Microdomains. Journal of Biological Chemistry. 283: 30015–30024.

18. Govardovskii, V., D. Korenyak, S. Shukolyukov, and L. Zueva. 2009. Lateral diffusion of rhodopsin in photoreceptor membrane: a reappraisal. Molecular Vision. 15: 1717–1729.

19. Najafi, M., M. Haeri, B. Knock, W. Schiesser, and P. Calvert. 2012. Impact of signaling microcompartment geometry on GPCR dynamics in live retinal photoreceptors. Current Biology. 23: 1–18.

20. Pugh, E., and T. Lamb. 1993. Amplification and kinetics of the activation steps in phototransduction. Biochim Biophys Acta. 1141: 111–149.

21. Erban, R., and S.J. Chapman. 2009. Stochastic modelling of reaction-diffusion processes: algorithms for bimolecular reactions. Physical biology. 6: 046001.

22. Fotiadis, D., Y. Liang, S. Filipek, D. Saperstein, A. Engel, et al. 2003. Atomic-force microscopyRhodopsin dimers in native disc membranes. Nature. 421: 127–128.